



## Article

# Reducing the Influence of Systematic Errors in Interference Core of Stepped Micro-Mirror Imaging Fourier Transform Spectrometer: A Novel Calibration Method

Baixuan Zhao<sup>1</sup>, Jingqiu Liang<sup>1</sup>, Jinguang Lv<sup>1,\*</sup>, Kaifeng Zheng<sup>1</sup>, Yingze Zhao<sup>1</sup>, Yupeng Chen<sup>1</sup>, Kaiyang Sheng<sup>1,2</sup>, Yuxin Qin<sup>1</sup> and Weibiao Wang<sup>1</sup>

<sup>1</sup> Changchun Institute of Optics, Fine Mechanics and Physics, Chinese Academy of Sciences, Changchun 130033, China

<sup>2</sup> Daheng College, University of Chinese Academy of Sciences, Beijing 100049, China

\* Correspondence: lvjg@ciomp.ac.cn

**Abstract:** The stepped micro-mirror imaging Fourier transform spectrometer (SIFTS) has the advantages of high throughput, compactness, and stability. However, the systematic errors in the interference core of the SIFTS have a significant impact on the interferogram and the reconstructed spectrum. In order to reduce the influence of systematic errors, a transfer error model of the systematic errors in the interference core of the SIFTS is established, and an interferogram and spectrum calibration method is presented, which combines the least squares fitting calibration and the row-by-row fast Fourier transform-inverse fast Fourier transform (FFT-IFFT) flat-field calibration. The experimental results show that the methods can sufficiently reduce the influence of systematic errors in the interference core of the SIFTS, such as the interferogram fringe tilt, the peak position shift of the reconstructed spectrum, and the error of spectral response.

**Keywords:** imaging Fourier transform spectrometer; stepped micro-mirror; systematic errors; interferogram and spectral calibration



**Citation:** Zhao, B.; Liang, J.; Lv, J.; Zheng, K.; Zhao, Y.; Chen, Y.; Sheng, K.; Qin, Y.; Wang, W. Reducing the Influence of Systematic Errors in Interference Core of Stepped Micro-Mirror Imaging Fourier Transform Spectrometer: A Novel Calibration Method. *Remote Sens.* **2023**, *15*, 985. <https://doi.org/10.3390/rs15040985>

Academic Editor: Amin Beiranvand Pour

Received: 6 December 2022

Revised: 28 January 2023

Accepted: 8 February 2023

Published: 10 February 2023



**Copyright:** © 2023 by the authors. Licensee MDPI, Basel, Switzerland. This article is an open access article distributed under the terms and conditions of the Creative Commons Attribution (CC BY) license (<https://creativecommons.org/licenses/by/4.0/>).

## 1. Introduction

Imaging Fourier transform spectroscopy (IFTS) can simultaneously acquire two-dimensional spatial information and one-dimensional spectral information [1–3], and has a high spectral resolution, high throughput, high stability, strong targeting, high sensitivity, strong adaptability, long service life, and other advantages [4–6], so it is widely used in environmental monitoring and atmospheric remote sensing and other fields [7–13]. Based on the structure of the Michelson interferometer, we proposed a stepped micro-mirror imaging Fourier transform spectrometer (SIFTS), which greatly improves stability and ensures high throughput and a certain spectral resolution [14–16].

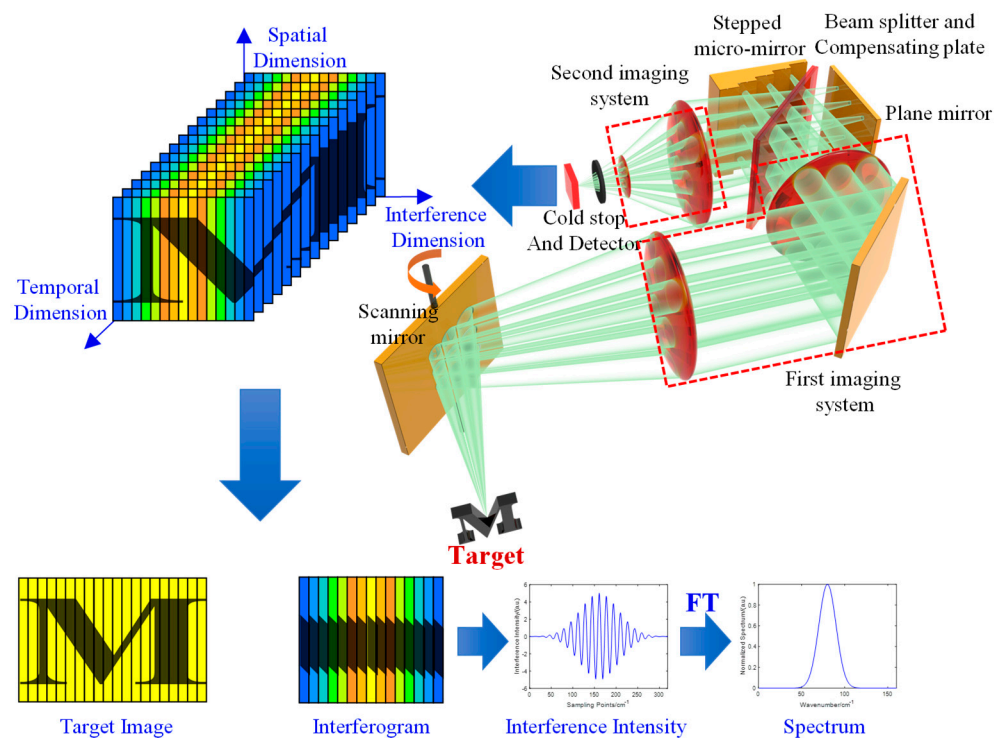
As an interferometric hyperspectral analysis instrument, the SIFTS has extremely high requirements for the assembly and adjustment accuracy of each component, especially the interference core composed of the plane mirror, the stepped micro-mirror, the beam splitter, and the compensation plate. The micron-level optical misalignment in the interference core will cause large systematic errors in the interferogram and the reconstructed spectrum. Since the installation accuracy of the beam splitter and the compensation plate is highly related to the processing accuracy of the interference core frame, the optical misalignment can be controlled within a negligible range. However, due to the large adjustable dimensions and difficulty of the assembly and adjustment of the stepped micro-mirror and plane mirrors, there will be some inevitable small optical misalignments, which require large, high-precision optical mounts and very careful alignment to calibrate. These calibration measures greatly increase the difficulty of assembly and adjustment, and affect the compactness and stability of the SIFTS. Therefore, a calibration method in the post-processing stage is needed to reduce the influence of these systematic errors.

There have been some research reports on the systematic error correction of interferometric spectrometers. Xiang et al. systematically analyzed the influence of the moving mirror tilt in the Fourier transform spectrometer on the degree of interference modulation and phase [17]. Gao et al. analyzed the influence of the rotating mirror tilt in the rotating mirror interference spectrometer on the degree of interference modulation and phase [18]. Zeng et al. analyzed the influence of different tilt directions of the moving mirror in the Fourier transform spectrometer on the system error [19]. Liu et al. analyzed the influence of the error of the tilt mirror in the spatial modulation Fourier transform spectrometer on the phase, spectral resolution, and signal-to-noise ratio [20]. Feng et al. analyzed the influence of the tilt error of the moving mirror on the circular aperture in the Fourier transform spectrometer, and proposed a dynamic calibration method [21]. Barnett et al. proposed a method to calibrate the interference fringe error [22]. Jin et al. analyzed the effect of detector alignment error on spectral resolution and gave error tolerance limits [23]. Zou et al. proposed a spectral fitting calibration method based on spectral refinement [24]. Feng et al. analyzed the reference atmospheric radiation transmission pattern and proposed a Fourier transform spectrometer on-orbit spectral calibration method [25]. Cui et al. proposed a radiation calibration method for micro spectrometer based on the Lagrangian interpolation algorithm [26]. Lv et al. proposed a radiation calibration method based on reflectivity parameters, simulation data and in-orbit measurement data comparison [27].

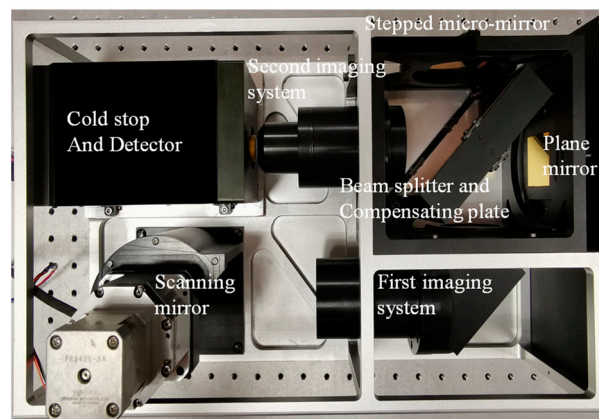
It can be seen that the current related research has mainly analyzed the influence of the systematic error in the interference system on the spectral phase and has seldom analyzed the influence of the systematic error on the spectral wavenumber. As well, the current research related to interferogram and spectral calibration methods is mainly for the improvement of traditional calibration methods in applications, and lacks integration with the analysis of systematic error modulation and transmission mechanisms of instruments. The special structure of the SIFTS interference core (the stepped micro-mirror) makes the systematic error have a significant impact on the spectral wavenumber and the interferogram. Therefore, in order to improve the measurement accuracy and reduce the difficulty of installation and adjustment, the relationship between the systematic error in the interference core of SIFTS and the spectral wavenumber error and the interferogram is analyzed in this paper. First, by analyzing the optical misalignment of the interference core, a transfer error model of the systematic error is established. Then, according to the transfer error model, an interferogram and spectrum calibration method combining least squares fitting correction and row-by-row fast Fourier transform-inverse fast Fourier transform (FFT-IFFT) flat-field correction is presented, which can reduce the influence of the systematic error in the interference system on the interferogram and the reconstructed spectrum, and reduce the difficulty of assembly and adjustment. Finally, in order to verify the method, we built an experimental verification platform and conducted verification experiments. The experimental results show that the method has a relatively good correction effect on various problems caused by the systematic error in the interference core of the SIFTS, such as the interferogram fringe tilt, the peak position shift of the reconstructed spectrum, and the spectral response error.

## 2. The Structure and Working Principle of SIFTS

Figure 1a shows the simplified configuration and mechanism for obtaining information about the SIFTS. Figure 1b shows the internal structure of the principle prototype, including a scanning mirror, a first imaging system, a plane mirror, a beam splitter, a compensation plate, a stepped micro-mirror, a second imaging system, and a detector with a cold stop.



(a)



(b)

**Figure 1.** (a) Simplified configuration and mechanism for obtaining information about the SIFTS; (b) internal structure of the prototype.

The working principle of the SIFTS is that at a certain time, the light emitted by the target object passes through the scanning mirror and first imaging system, forming two primary image points on the plane mirror and the stepped micro-mirror, respectively. The two primary image points are ultimately imaged through the second imaging system on the focal plane of the detector, after being reflected by the plane mirror and micro-mirror. The difference in height between the plane mirror and micro-mirror causes the optical path differences (OPDs) between the two beams reaching the detector, thereby forming interference fringes on the detector. Therefore, image and spectral information regarding the target reaches the detector. Then the scanning mirror rotates, and the target is imaged on the next step surface, so the detector can obtain interference information concerning the

different OPDs of the target. The interference intensity distribution can be expressed in the following form:

$$I(\delta) = \int_{-\infty}^{+\infty} B(\nu) \exp(i2\pi\nu\delta) d\nu \quad (1)$$

where  $\nu$  is the wave number of the incident light,  $\delta$  is the OPD of the SIFTS system, and  $B(\nu)$  is the power spectral density of the incident light. The input spectrum can be obtained by Fourier transform:

$$B(\nu) = \int_{-\infty}^{+\infty} I(\delta) \exp(-i2\pi\nu\delta) d\delta \quad (2)$$

After one scan period, the detector obtains a three-dimensional data cube containing two-dimensional spatial information and one-dimensional spectral information. The IR images and spectra of the target are obtained by demodulating and processing the interference data for the data cubes according to the scanning order and OPD order.

The interference core of the SIFTS uses a stepped micro-mirror, which has 128 substeps with a height of  $0.625 \mu\text{m}$  and a width of  $0.25 \text{ mm}$ , thereby obtaining a theoretical spectral resolution of  $62.5 \text{ cm}^{-1}$ . The SIFTS uses a mid-wave infrared HgCdTe area array detector with a response spectrum of  $3.7\sim 4.8 \mu\text{m}$ , the number of pixels is  $320 \times 256$ , and the pixel size is  $30 \mu\text{m} \times 30 \mu\text{m}$ .

### 3. Transfer Error Model of the Interference Core

The establishment of the transfer error model of the interference core requires a clear definition of the source of the error and its functional relationship with the interferogram or the reconstructed spectrum. Figure 2 shows the corresponding relationship between the two dimensions of the interferogram and the two dimensions of the stepped micro-mirror and the plane mirror, as well as the main source of the interference core systematic error (the black part in Figure 2b represents the stepped micro-mirror, and the red part represents the virtual image of the plane mirror).

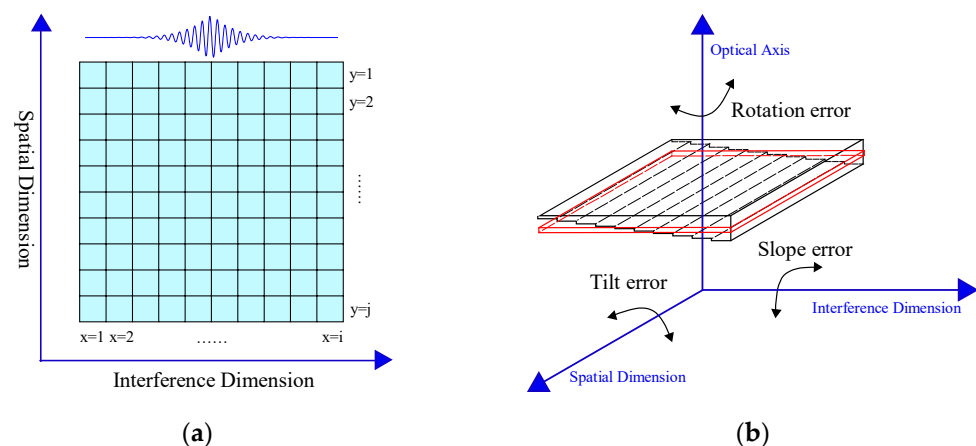


**Figure 2.** (a) Schematic diagram of interferogram measured by SIFTS. (b) Schematic diagram of the error classification in interference core.

As shown in Figure 2a, the interferogram of the SIFTS can be divided into two dimensions. The lateral interference dimension is modulated by the OPD sequence, which corresponds to the height change direction of the stepped micro-mirror in Figure 2b. The longitudinal spatial dimension corresponds to the longitudinal coordinates of the stepped micro-mirror and the virtual image of the plane mirror in Figure 2b. As shown in Figure 2b, the systematic errors of the interference core all come from the misalignment of the stepped micro-mirror and the plane mirror in different dimensions. Since the error introduced by

the misalignment of the stepped micro-mirror and the plane mirror in the same dimension are similar, the errors of the two elements can be combined and analyzed. Therefore, the systematic error of the interference core can be divided into three categories: tilt error, slope error, and rotation error.

### 3.1. Tilt Error

Suppose the ideal spatial sampling interval (twice the height of the stepped micro-mirror) is  $\delta_0$ , and the spatial interference dimension coordinate is  $x$ , then OPD can be expressed as a function of  $x$ :  $\delta = \delta_0 \cdot x$ . Figure 3 shows the simplified model of the tilt error analysis of a stepped micro-mirror or a plane mirror. Suppose the tilt angle is  $\alpha$ , the distance between the reflecting surface and the detector array is  $L$ , and the interference dimension coordinate of the tilt axis center is  $x_0$ .

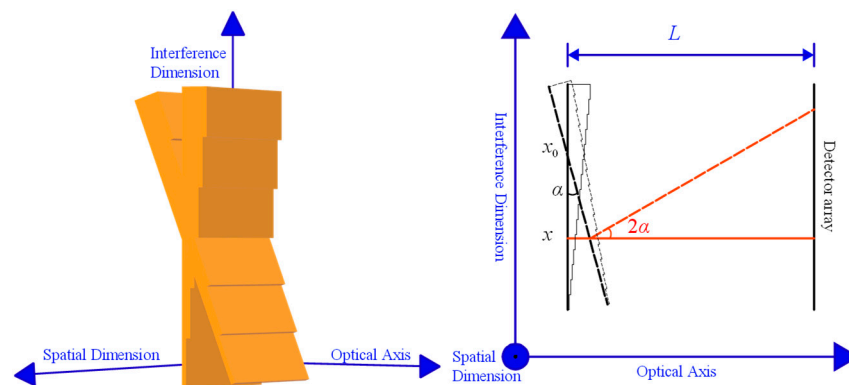


Figure 3. Tilt error structure.

When the stepped micro-mirror or flat mirror has a tilt error, its reflecting surface deviates from the standard position of the interference dimension, and the incident light will also deviate from the optical axis direction after being reflected by the reflecting surface, thus introducing an OPD error  $\epsilon_x$  at each sampling position of the spatial interference dimension. According to the geometric relationship in Figure 3,  $\epsilon_x$  can be expressed as a function of the interference dimension coordinate  $x$ :

$$\epsilon_x = x \tan \alpha \left( \frac{\cos 2\alpha + 1}{\cos 2\alpha} \right) + \left[ \left( \frac{2 \cos 2\alpha - 1}{\cos 2\alpha} \right) L - x_0 \tan \alpha \left( \frac{\cos 2\alpha + 1}{\cos 2\alpha} \right) \right] \quad (3)$$

Then the OPD after introducing the tilt error is:

$$\delta' = \delta + \epsilon_x = \frac{\delta_0 + \tan \alpha \left( \frac{\cos 2\alpha + 1}{\cos 2\alpha} \right)}{\delta_0} \cdot \delta + \frac{(2 \cos 2\alpha - 1)L - x_0 \tan \alpha (\cos 2\alpha + 1)}{\cos 2\alpha} \quad (4)$$

In addition, we can see in Figure 3 that the existence of the tilt angle will make the structure of the stair-step micro-mirror resemble a blazed grating, causing the incident light to be diffracted onto the stepped micro-mirror, so that the fundamental frequency of the interference fringe spatial frequency changes from 0 to the Littrow wave number (the Littrow wave number is determined by the Littrow angle, that is, the tilt angle  $\alpha$  of the stepped micro-mirror) [28–30]. Then, the interference intensity distribution becomes:

$$I'(\delta) = \int_{-\infty}^{+\infty} B(\nu) \exp[i2\pi2(\nu - \nu_{Littrow}) \tan \alpha \delta'] d\nu \quad (5)$$

Substituting Equation (4) into Equation (5), we can obtain:

$$I'(\delta) = \int_{-\infty}^{+\infty} B(\nu) \exp(i2\pi2(\nu - \nu_{Littrow}) \tan \alpha \left[ \frac{\delta_0 + \tan \alpha \left( \frac{\cos 2\alpha + 1}{\cos 2\alpha} \right)}{\delta_0} \cdot \delta + \frac{(2 \cos 2\alpha - 1)L - x_0 \tan \alpha (\cos 2\alpha + 1)}{\cos 2\alpha} \right]) d\nu \tag{6}$$

Equation (6) can be further organized to obtain:

$$B'(\nu) = B \left\{ \frac{\nu - 2\nu_{Littrow} \tan \alpha \left[ 1 + \frac{1}{\delta_0} \tan \alpha \left( \frac{\cos 2\alpha + 1}{\cos 2\alpha} \right) \right]}{1 - 2 \tan \alpha \left[ 1 + \frac{1}{\delta_0} \tan \alpha \left( \frac{\cos 2\alpha + 1}{\cos 2\alpha} \right) \right]} \right\} \times \exp \left\{ i2\pi2 \frac{(\nu - \nu_{Littrow}) \left( \frac{2 \cos 2\alpha - 1}{\cos 2\alpha} \right) L - x_0 \tan \alpha (\cos 2\alpha + 1)}{1 - 2 \tan \alpha \left[ 1 + \frac{1}{\delta_0} \tan \alpha \left( \frac{\cos 2\alpha + 1}{\cos 2\alpha} \right) \right]} \tan \alpha \right\} \tag{7}$$

It can be seen that the tilt error changes the frequency domain sampling interval and introduces a fixed wavenumber drift and a certain phase error. The phase error will not affect the mode of the spectrum, so it can be ignored in the process of spectrum calibration. However, the change in the frequency domain sampling interval and the fixed wavenumber drift will have a greater impact on the accuracy of the peak position of the spectrum, and calibration is required. According to Equation (7), the wavenumber change after introducing the tilt error can be obtained:

$$\nu_{Tilt} = \frac{\nu}{1 - 2 \tan \alpha \left[ 1 + \frac{1}{\delta_0} \tan \alpha \left( \frac{\cos 2\alpha + 1}{\cos 2\alpha} \right) \right]} - \frac{2\nu_{Littrow} \tan \alpha \left[ 1 + \frac{1}{\delta_0} \tan \alpha \left( \frac{\cos 2\alpha + 1}{\cos 2\alpha} \right) \right]}{1 - 2 \tan \alpha \left[ 1 + \frac{1}{\delta_0} \tan \alpha \left( \frac{\cos 2\alpha + 1}{\cos 2\alpha} \right) \right]} \tag{8}$$

Except for  $\nu_{Tilt}$  and  $\nu$ , all the others in Equation (8) are constants. In order to simplify the subsequent calculation, Equation (8) can be written as follows:

$$\nu_{Tilt} = k_{Tilt}\nu + b_{Tilt} \tag{9}$$

where  $k_{Tilt}$  and  $b_{Tilt}$  are the transfer error coefficients, and the specific values are:

$$\begin{cases} k_{Tilt} = \frac{1}{1 - 2 \tan \alpha \left[ 1 + \frac{1}{\delta_0} \tan \alpha \left( \frac{\cos 2\alpha + 1}{\cos 2\alpha} \right) \right]} \\ b_{Tilt} = - \frac{2\nu_{Littrow} \tan \alpha \left[ 1 + \frac{1}{\delta_0} \tan \alpha \left( \frac{\cos 2\alpha + 1}{\cos 2\alpha} \right) \right]}{1 - 2 \tan \alpha \left[ 1 + \frac{1}{\delta_0} \tan \alpha \left( \frac{\cos 2\alpha + 1}{\cos 2\alpha} \right) \right]} \end{cases} \tag{10}$$

### 3.2. Slope Error

Figure 4 shows the simplified slope error analysis model of a stepped micro-mirror or a plane mirror. Suppose the slope angle is  $\beta$ , the distance between the reflecting surface and the detector array is  $L$ , and the spatial dimension coordinate of the slope axis is  $y_0$ .

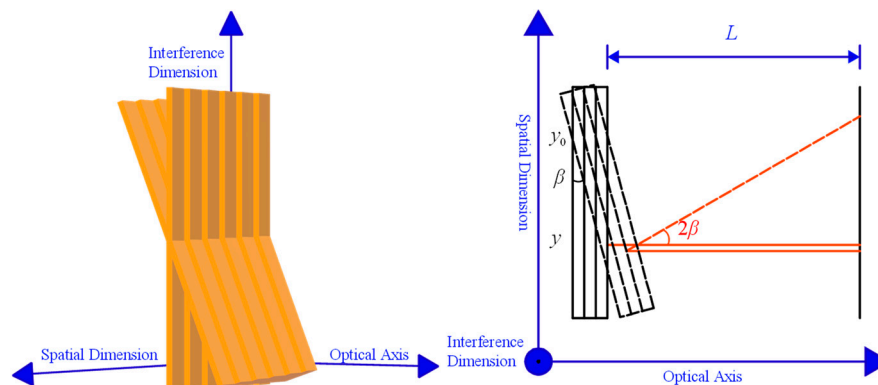


Figure 4. Slope error structure.

When we only consider the slope error of the stepped micromirror or plane mirror, the reflecting surface will also deviate from the standard position of the interference dimension, so that the incident light will deviate from the optical axis direction after being reflected by the reflecting surface, but the offset only changes with the spatial dimension coordinates. According to the geometric relationship in Figure 4, the slope error can be expressed as:

$$\varepsilon_y = y \tan \beta \left(1 + \frac{1}{\cos 2\beta}\right) - (L - y_0 \tan \beta) \left(1 + \frac{1}{\cos 2\beta}\right) + 2L \quad (11)$$

The spatial sampling interval has also changed:

$$\delta_0' = \delta_0 \frac{1 + \cos 2\beta}{\cos \beta} \quad (12)$$

Substituting  $\varepsilon_y$  and  $\delta_0'$  into Equation (1), we can obtain:

$$I'(\delta) = \int_{-\infty}^{+\infty} B(v) \exp\{i2\pi v [\delta_0 \frac{1 + \cos 2\beta}{\cos \beta} + y \tan \beta \left(1 + \frac{1}{\cos 2\beta}\right) - (L - y_0 \tan \beta) \left(1 + \frac{1}{\cos 2\beta}\right) + 2L]\} dv \quad (13)$$

Equation (13) can be further organized to obtain:

$$B'(v) = B\left(v \frac{\cos \beta}{1 + \cos 2\beta}\right) \exp[i2\pi v \frac{\cos \beta}{1 + \cos 2\beta} + y \tan \beta \left(1 + \frac{1}{\cos 2\beta}\right) - (L - y_0 \tan \beta) \left(1 + \frac{1}{\cos 2\beta}\right) + 2L] \quad (14)$$

It can be seen that the slope error changes the frequency domain sampling interval and introduces a certain phase error. Similar to the case of the tilt error, ignoring the phase error, the wavenumber relationship before and after the slope error can be obtained:

$$v_{Slope} = \frac{\cos \beta}{1 + \cos 2\beta} v \quad (15)$$

Except for  $v_{Slope}$  and  $v$ , all the other variables in Equation (15) are constants. In order to simplify the subsequent calculation, Equation (15) can be written as follows:

$$v_{Slope} = k_{Slope} v \quad (16)$$

where  $k_{Slope}$  is the transfer error coefficients, and the specific values is:

$$k_{Slope} = \frac{\cos \beta}{1 + \cos 2\beta} \quad (17)$$

### 3.3. Rotation Error

Figure 5 shows the simplified rotation error analysis model of a stepped micro-mirror or a plane mirror. Suppose the rotation angle is  $\gamma$ , and the rotation center coordinate is  $(x_\gamma, y_\gamma)$ .

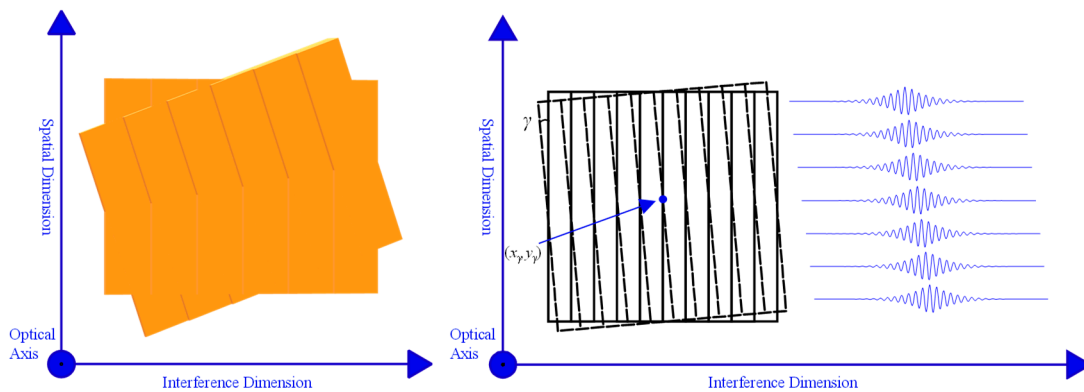


**Figure 5.** Rotation error structure.

It can be seen that the rotation error will not introduce the OPD error but will cause the overall translation of the interference sequence of each row, that is, the rotation of the interference fringes. The translation of the interference sequence can be expressed as:

$$\Delta x = x - x_\gamma = (y - y_\gamma) \tan \gamma \tag{18}$$

According to the Fourier transform displacement theorem [31], the effect of the interference sequence translation on the spectrum can be expressed as:

$$B'(v) = \mathcal{F}\{I[(x - (y - y_\gamma) \tan \gamma)\delta_0]\} = B(v) \exp[-i2\pi\delta_0x(y - y_\gamma) \tan \gamma] \tag{19}$$

Equation (17) shows that the rotation error will not bring about a frequency shift, but only a phase shift, so it can be ignored in the spectral calibration. However, in the radiation calibration, it is necessary to calibrate the relative radiation response of the pixels of the same interference order, and the rotation of the fringes will cause the pixels in the same column in the longitudinal direction to no longer be in the same interference order, so the difficulty of calibrating the relative radiation response between the pixels of the same interference order is greatly increased.

### 3.4. Transfer Error Model

The analysis in Sections 3.1–3.3 shows that the major influences on the spectrum are the tilt error and the slope error, and the wavenumber shift caused by these two errors is linear, which can be organized into a transfer error model:

$$v' = kv + b \tag{20}$$

where  $k$  and  $b$  are the transfer error coefficients, and the specific values are:

$$\begin{cases} k = k_{Tilt} + k_{Slope} = \frac{1}{1 - 2 \tan \alpha [1 + \frac{1}{\delta_0} \tan \alpha (\frac{\cos 2\alpha + 1}{\cos 2\alpha})]} + \frac{\cos \beta}{1 + \cos 2\beta} \\ b = b_{Tilt} = -\frac{2v_{Littrow} \tan \alpha [1 + \frac{1}{\delta_0} \tan \alpha (\frac{\cos 2\alpha + 1}{\cos 2\alpha})]}{1 - 2 \tan \alpha [1 + \frac{1}{\delta_0} \tan \alpha (\frac{\cos 2\alpha + 1}{\cos 2\alpha})]} \end{cases} \tag{21}$$

It can be seen that the transfer error model is a linear form. Due to the high integration of the SIFTS interference core, some precision measurement tools are difficult to apply and the parameters in Equation (21) are very difficult to measure. Therefore, in the calibration process, it is only necessary to measure the peak wavenumbers of at least two standard narrowband radiation sources with different central wavenumbers, and substitute them into Equation (20) together with the theoretical central wavenumbers to obtain the transfer error coefficients  $k$  and  $b$ , and then complete for wavenumber calibration, there is no need to calculate the parameters in Equation (21).

### 4. Calibration Method and Experimental Design

#### 4.1. Calibration Method

The calibration process of the static Fourier transform spectrometer is as follows [32,33]. First, the relative radiation response between the pixels of the same interference order of the interferogram is calibrated in the spatial domain. Then, spectral calibration is performed, and finally, spectral responsivity is calibrated in the frequency domain. It can be seen in Section 3 that the systematic errors of the interference core mainly cause the fringe rotation of the interferogram and the wavenumber shift of the spectrum. The rotation of the interference fringes will cause the pixels in the same column in the longitudinal direction to no longer be in the same interference order, so the difficulty of calibrating the relative radiation response between the pixels of the same interference order is greatly increased. The wavenumber shift of the spectrum will increase the difficulty of spectral calibration, which in turn affects the spectral responsivity calibration in the frequency domain.

Aiming at the influence of the systematic error of the interference core, we propose a new calibration method, based on the transfer error model in Section 3 and combined with the least squares method and progressive FFT-IFFT to calibrate the interference data. The calibration flow chart is shown in Figure 6:

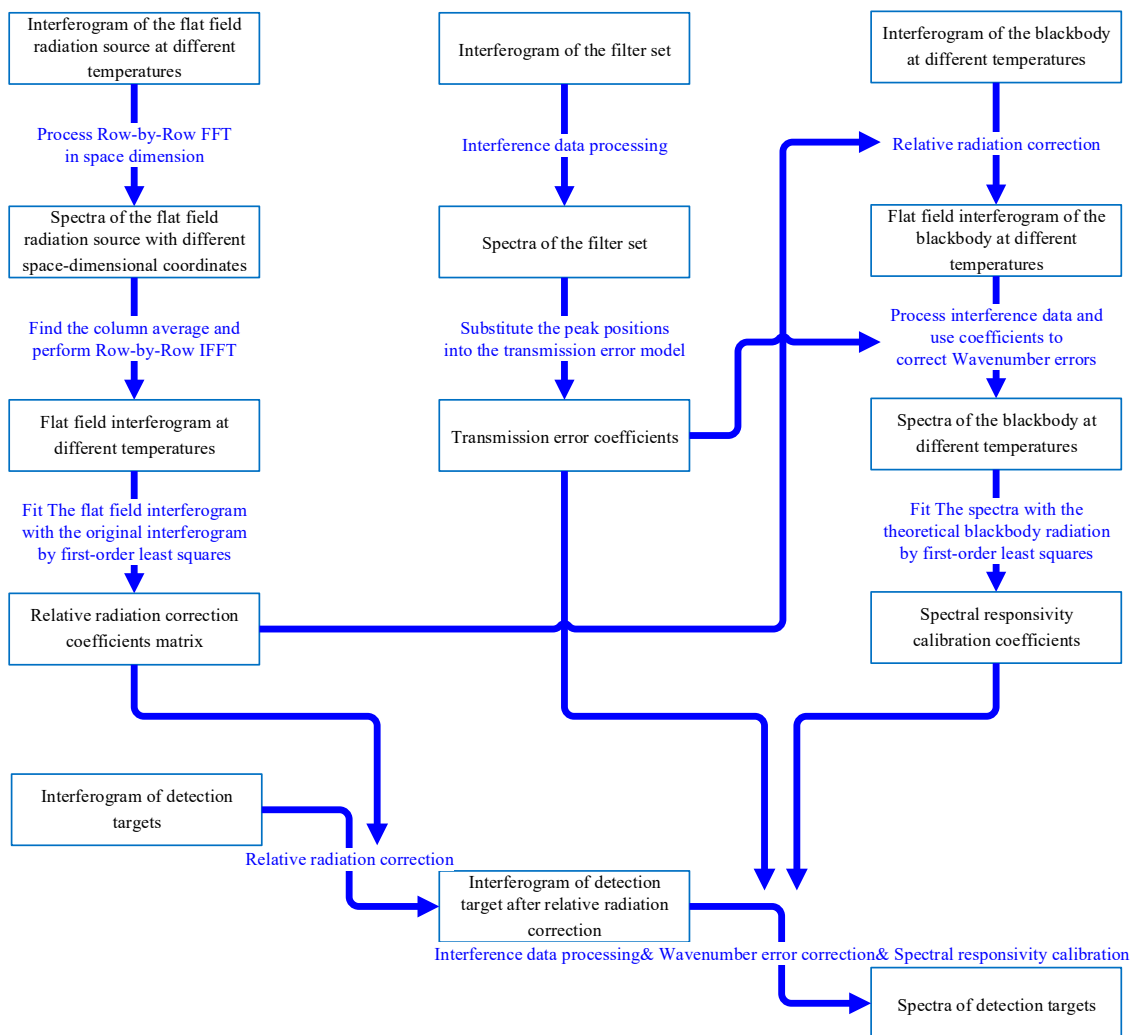


Figure 6. Calibration flow chart.

The calibration process can be mainly divided into three parts. The first part is the calibration of the relative radiation response of the pixels of the same interference order,

the second part is the calibration of the spectral wavenumber, and the third part is the calibration of the spectral responsivity.

The first part is the calibration of the relative radiation response of the pixels of the same interference order. Aiming at the rotation of the interference fringes caused by the rotation error, we propose a row-by-row FFT-IFFT relative radiation response calibration method. First, measure the interferograms of flat-field radiation sources with different temperatures. Due to the possible rotation error of the interference core, the interference fringes will have a certain rotation, which causes the pixels of the same interference order to no longer be in the same column, which cannot be solved by averaging the columns. According to the analysis in Section 3.3, the rotation error will cause the overall translation of the interference sequence of each row, thereby introducing a phase shift in the frequency domain without introducing a wavenumber shift. Therefore, the interferogram can be subjected to row-by-row fast Fourier transform, and the column average can be obtained after transforming to the frequency domain, and then the inverse Fourier transform IFFT can be performed to obtain the interferogram corresponding to the calibration of the relative radiation, as shown in Figure 7. Finally, the interferograms of the corrected flat-field radiation sources with different temperatures and the original interferograms are fitted by the pixel-by-pixel first-order least squares method to obtain the relative radiation response calibration coefficient matrix.

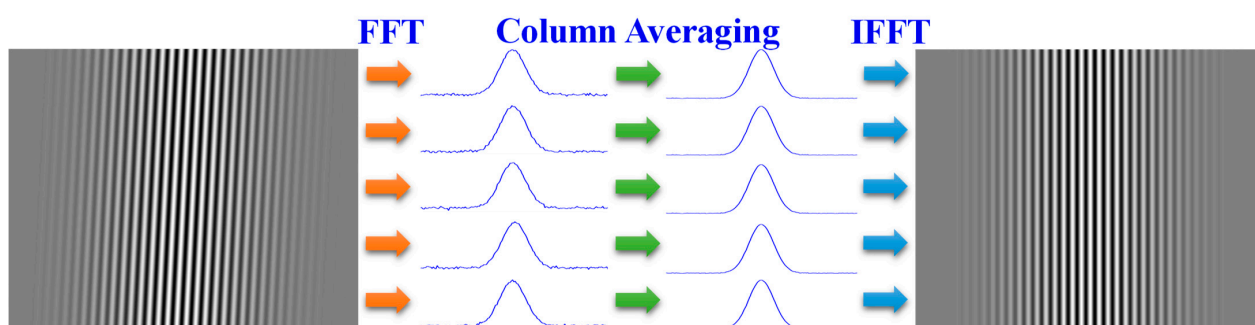


Figure 7. Row-by-row FFT-IFFT.

In the second part of the spectral wavenumber calibration, according to the analysis in Sections 3.1 and 3.2, the systematic error of the interference core will cause the spectral wavenumber to drift linearly. According to the specific form of the transfer error model, a group of standard narrowband radiation sources with different central wavenumbers is selected, their interferograms are obtained, and the relative radiation response calibration coefficient matrix obtained in the first part is used for calibration. Then the interference data are processed to obtain the measured central wavenumber, and finally, first-order least squares fitting is performed with the theoretical central wavenumber to obtain the spectral transfer error coefficients  $k$  and  $b$ .

The third part is the spectral responsivity calibration. In this part, a temperature range and sampling interval are set, the instrument is used to obtain the interferogram of the blackbody corresponding to the temperature, and the relative radiation response calibration coefficient matrix obtained in the first part is used for calibration. Then the interference data are processed to obtain the blackbody spectrum, and the spectral error transfer coefficients  $k$  and  $b$  obtained in the second part are used to perform spectral calibration. Finally, the first-order least squares fitting is performed between the measured blackbody spectrum and the theoretical blackbody spectrum corresponding to the temperature, and the spectral response calibration coefficient can be obtained.

After all three calibration coefficients are obtained, the spectral data of any detection target can be calibrated.

#### 4.2. Experimental Design

According to the calibration method in Section 4.1, during the calibration experiment, we needed to measure mainly flat-field radiation sources with different temperatures, standard narrow-band radiation sources with different central wavenumbers, and standard blackbodies with different temperatures. Figure 8 shows the schematic and photograph of the laboratory calibration system of the SIFTS. The flat-field radiation source consisted of a calibrated standard point source blackbody and a beam expander system. The end of the beam expander system can add and replace narrow-band filters, which can simulate standard narrow-band radiation sources with different center wavelengths.

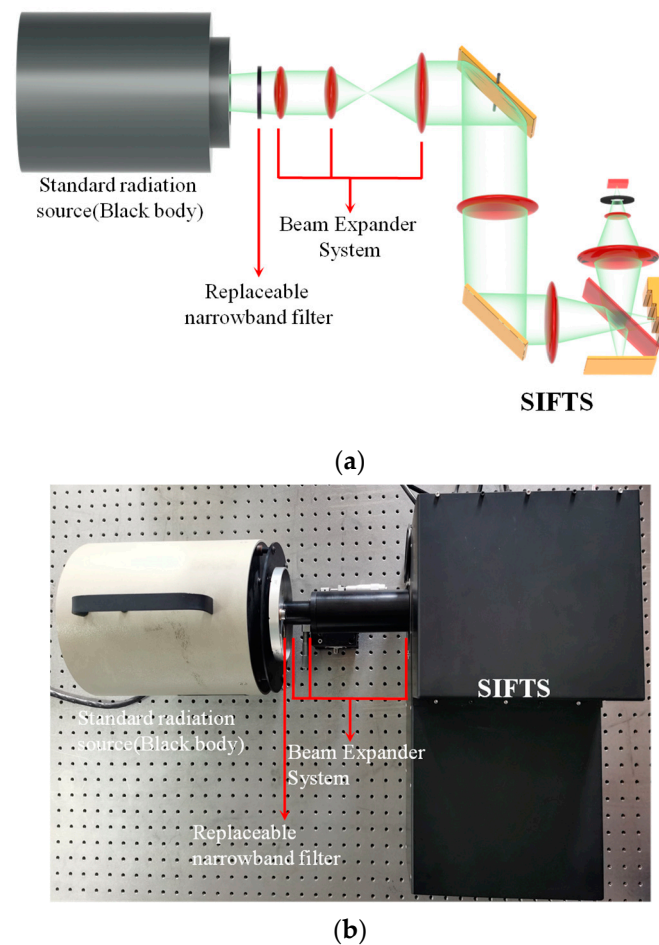


**Figure 8.** (a) Schematic of the laboratory calibration system. (b) Photograph of the laboratory calibration system with a layout corresponding to (a).

Figure 9 shows the image plane intensity distribution of the effective area of the point light source imaged by the beam expander system simulated by the simulation software. After calculation, the flatness of the effective imaging area of the image plane was 99.98%, which can basically be regarded as a flat-field radiation source.

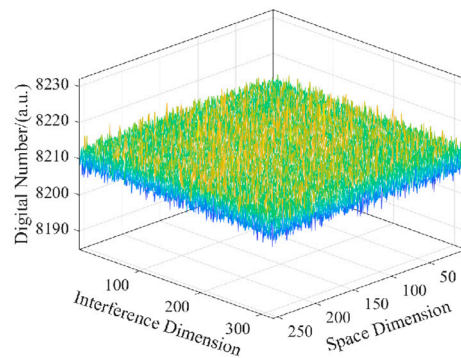


**Figure 9.** The intensity distribution of image plane of point light source imaging by the beam expander system.

After the calibration was complete, further verification of the calibration results was required. Considering the response band of the SIFTS, we used a liquid sample glass slide made of acetonitrile with a strong absorption peak around  $2273\text{ cm}^{-1}$  to verify the effect of spectral wavenumber calibration, and the standard blackbody spectrum of the temperature point not used in the calibration was used to verify the effects of relative radiation response calibration and the spectral response calibration.

## 5. Experimental Results and Discussion

### 5.1. Relative Radiation Response Calibration

We set 10 temperature points in the temperature range of 338 K–373 K (the temperature range is a common range for SIFTS in applications), measured the flat-field radiation source corresponding to the temperature, selected the effective interference area, and obtained the interferograms as shown in Figure 10:

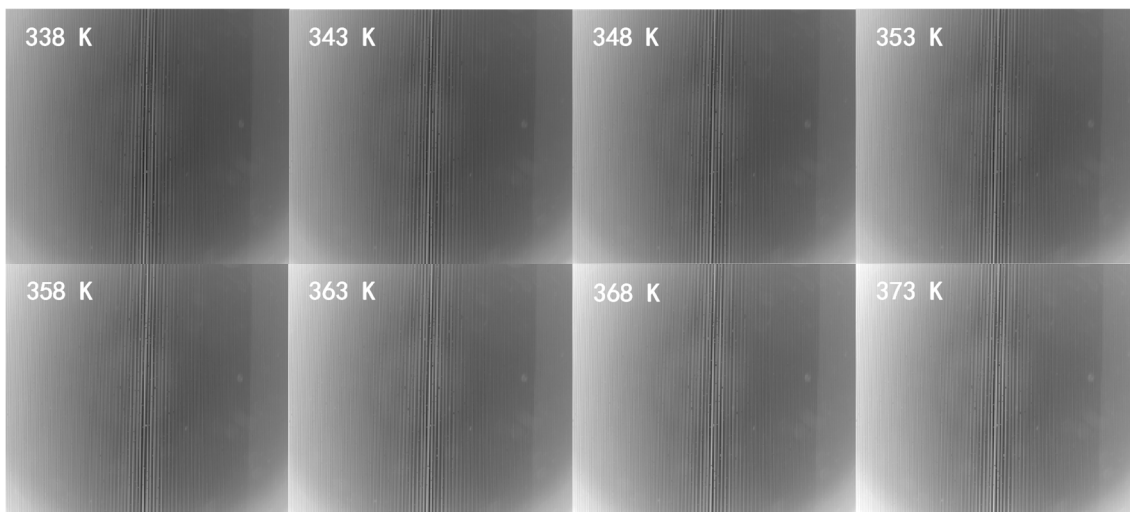


**Figure 10.** Interferograms of flat field radiation source in 338 K–373 K.

We took the interferogram of a 338 K radiation source as an example of the specific calibration process. In order to clearly show the characteristics of the interference data, the subsequent processing is displayed in pseudo-color. Figure 11 shows the two-dimensional interferogram of the 338 K radiation source and its three-dimensional curved surface.

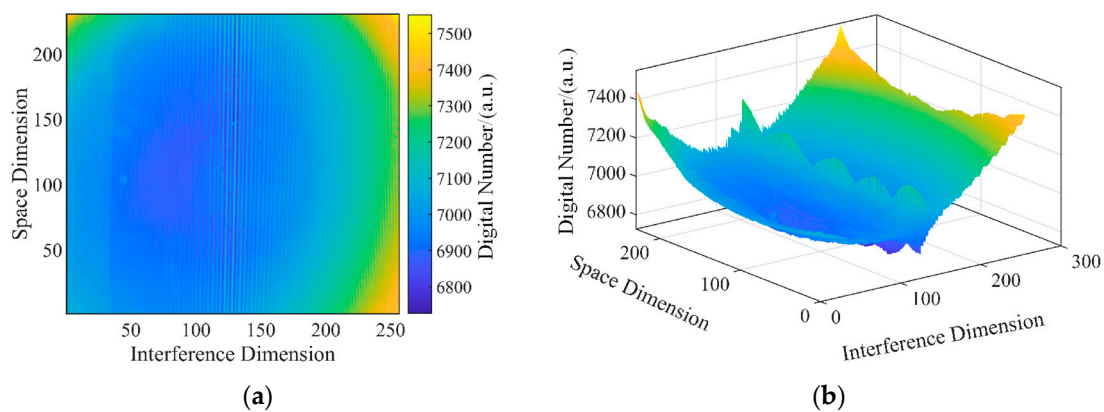


**Figure 11.** (a) Two-dimensional interferogram of 338 K radiation source. (b) Three-dimensional surface of the interferogram.

It can be seen that the interference fringes had obvious rotation, the baseline is greatly distorted, and the response uniformity of the pixels of the same interference order is poor. The relative radiation response calibration was performed using the row-by-row FFT-IFFT method proposed in Section 4.1. Since there were two pixels on an interference order in the interferometric dimension, the interferogram was split into two parts and processed separately. The frequency domain distribution obtained by row-by-row FFT, the frequency domain distribution after column averaging, and the corrected interferogram obtained after row-by-row IFFT are shown in Figure 12.

Figure 12a,b shows the spatial distribution of the one-dimensional spectrum obtained after baseline correction and the row-by-row FFT of the interference data of the flat-field radiation source on two pixels in the same order (the left-right symmetry is due to the conjugate symmetry effect of the Fourier transform). Since the rotation of the interference fringes had no effect on the peak position of the frequency domain spectrum, the column average could be directly obtained. Figure 12c,d shows the distribution of the one-dimensional spectrum in the spatial dimension after the column average. We performed row-by-row IFFT on Figure 12c,d and rearranged the same-level pixels to obtain Figure 12e,f, that is, the interferogram after relative radiation calibration. It can be seen that the rotation of the interference fringes and the poor uniformity of the response of the same interference order pixel were greatly improved. Then, the above-mentioned processing was performed on the interferogram of the flat-field radiation source corresponding to each temperature point, and finally, the calibration coefficient of the relative radiation response of each pixel was obtained by first-order least squares fitting, as shown in Figure 13:

### 5.2. Spectral Wavenumber Calibration

In this part, we selected a set of narrow-band filters with center wavelengths of 4.12  $\mu\text{m}$ , 4.275  $\mu\text{m}$ , 4.515  $\mu\text{m}$ , and 4.685  $\mu\text{m}$  (the half-peak widths are all smaller than the theoretical spectral resolution of the SIFTS), which were installed in the beam expander system. Then we measured their interferograms (blackbody temperature of 500 K). Finally, the interference data of the interferograms of the filter set were processed to obtain the spectra. The interferograms and spectra of the filter settings are shown in Figure 14:

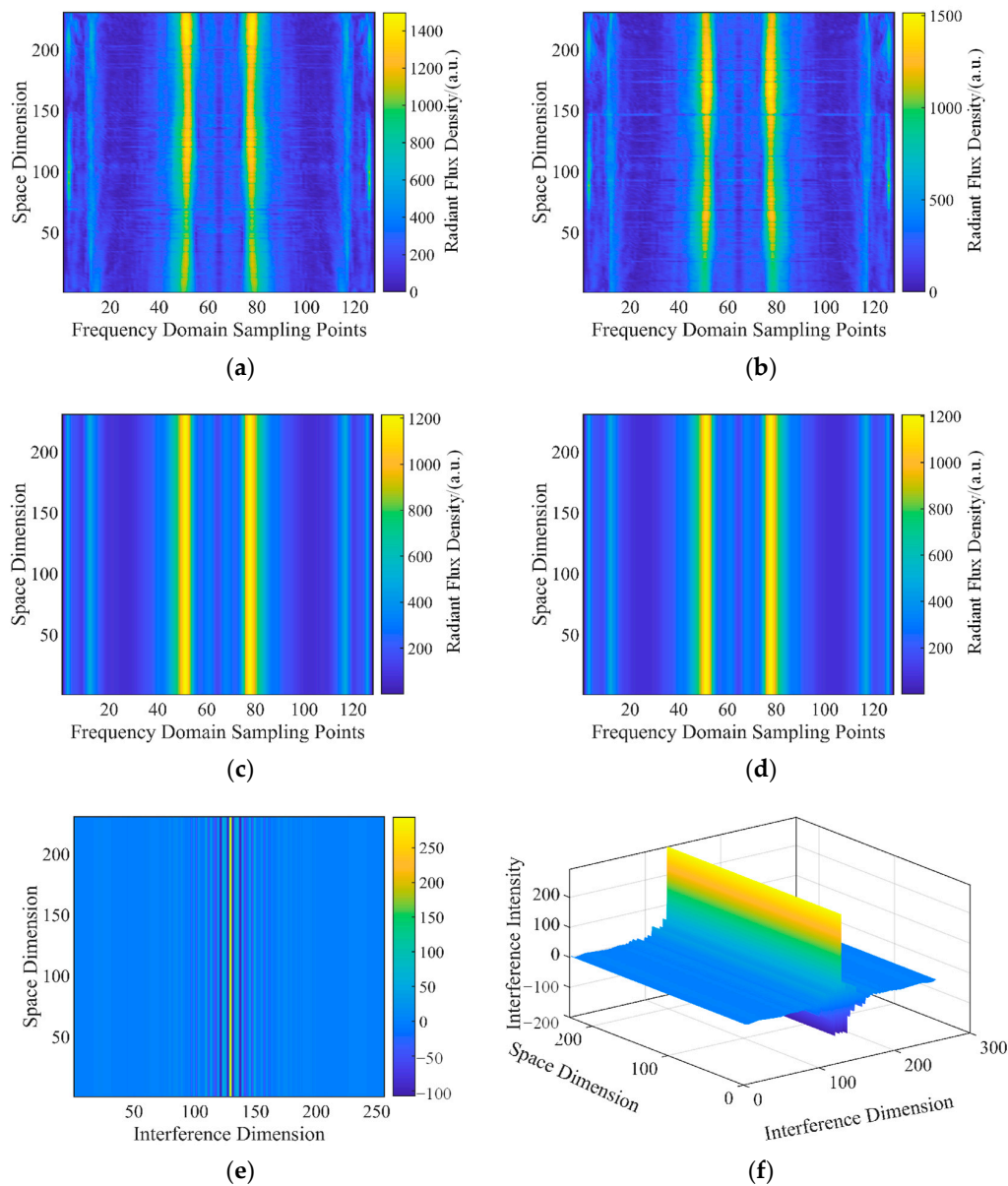


**Figure 12.** (a,b) Spectra of the flat field radiation source with different space-dimensional coordinates. (c,d) Column averaged spectra. (e) Two-dimensional interferogram after relative radiation correct. (f) Three-dimensional surface of the interferogram.

Due to the low theoretical spectral resolution of the SIFTS, in order to reduce the influence of the fence effect, the zero-padding method was used to increase the wavenumber accuracy of the spectrum in the process of the interference data processing, and the zero-padding multiple was selected to be 100 times. The measured spectral center wavenumbers of the filter set were  $2350.7 \text{ cm}^{-1}$ ,  $2562.7 \text{ cm}^{-1}$ ,  $2862.2 \text{ cm}^{-1}$ , and  $3055.6 \text{ cm}^{-1}$ , which have large errors with the theoretical values of  $2427.2 \text{ cm}^{-1}$ ,  $2339.2 \text{ cm}^{-1}$ ,  $2214.8 \text{ cm}^{-1}$ , and  $2134.5 \text{ cm}^{-1}$ . The central wavenumber of the filter set was substituted into the transfer error model, that is, Equation (20), and  $k$  was obtained as  $-0.4152$  and  $b$  as  $3403.3$ . Then, the transfer error model was obtained as:

$$\nu' = -0.4152\nu + 3403.3431 \quad (22)$$

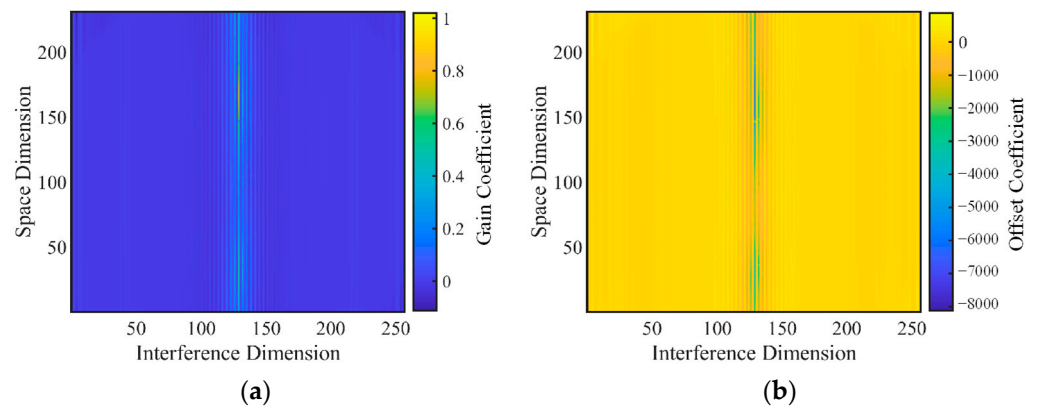
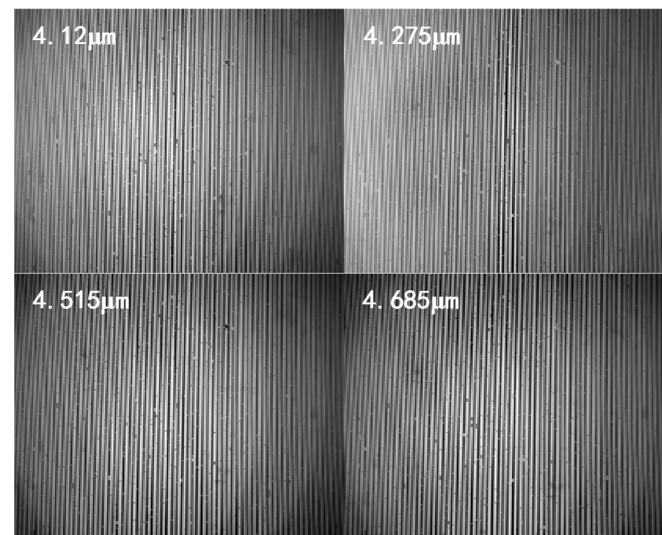
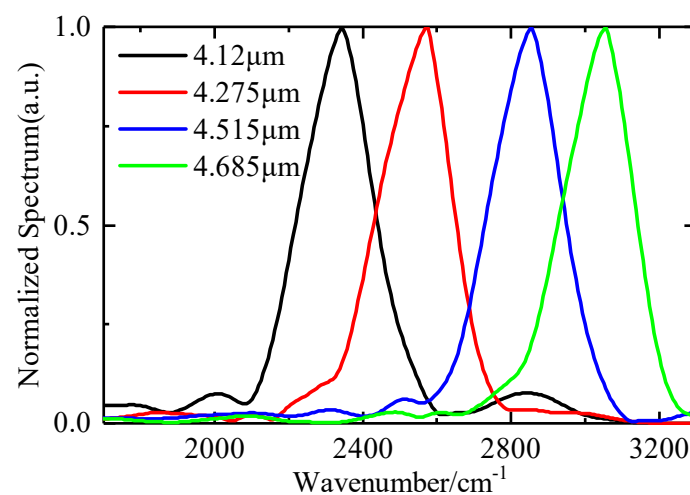


**Figure 13.** The calibration coefficient of the relative radiation response of each pixel. (a) Gain coefficient matrix. (b) Offset coefficient matrix.



(a)



(b)

**Figure 14.** (a) Interferograms of filter set. (b) Normalized spectra of filter set.

The transfer error model was used to calibrate the filter set spectra, and the filter set spectra were obtained after the spectral wavenumber calibration, as shown in Figure 15:

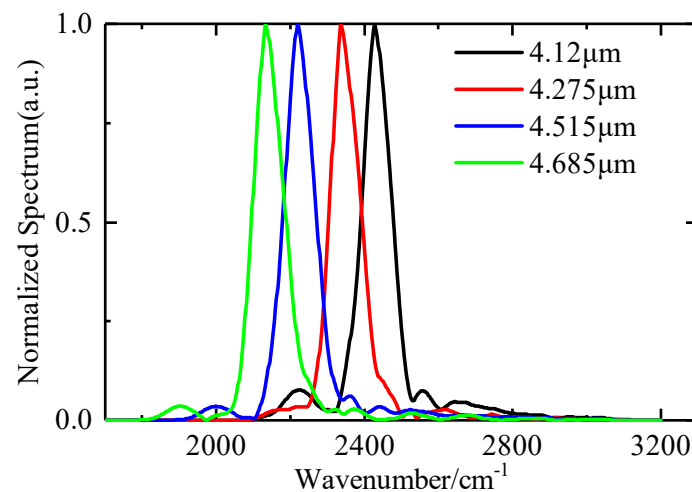


**Figure 15.** Normalized spectra of filter set after wavenumber calibration.

The central wavenumbers of the calibrated spectrum were  $2427.3 \text{ cm}^{-1}$ ,  $2339.3 \text{ cm}^{-1}$ ,  $2214.9 \text{ cm}^{-1}$ , and  $2134.7 \text{ cm}^{-1}$ , and the average error from the theoretical value was only 0.0056%. Moreover, it can be seen that the systematic error of the interference core not only introduced a large wavenumber error but also caused a serious broadening of the spectrum, which greatly reduced the resolution. The wavenumber calibration can simultaneously calibrate the wavenumber error and spectral broadening.

### 5.3. Spectral Response Calibration

In this section, we continue to use the data measured in the relative radiation response calibration, performing a relative radiation calibration of the interferogram using the relative radiation response calibration coefficient matrix obtained in Section 5.1, and then perform the interference data processing, using the transfer error model obtained in Section 5.2 to perform the wavenumber calibration to obtain the spectral responses of blackbodies at different temperatures. The spectral response calibration coefficient can be obtained by fitting the measured blackbody spectral response with the theoretical blackbody radiation by the first-order least squares method. The measured spectral response of the blackbody at different temperatures, the theoretical blackbody radiation, the spectral response calibration coefficient, and the calibrated blackbody spectral response are shown in Figure 16:

Figure 16 shows that the relative error between the blackbody spectrum after the spectral response calibration and the theoretical value was 1.32%.

### 5.4. Verification of Calibration Methods

In this section, we verify the calibration method. According to the experimental design in Section 4.2, we used a liquid sample glass slide made of acetonitrile with a strong absorption peak around  $2273 \text{ cm}^{-1}$  to verify the effect of the spectral wavenumber calibration, and used the standard blackbody spectrum of 333 K to verify the effects of the relative radiation response calibration and the spectral response calibration. The results obtained are shown in Figure 17:

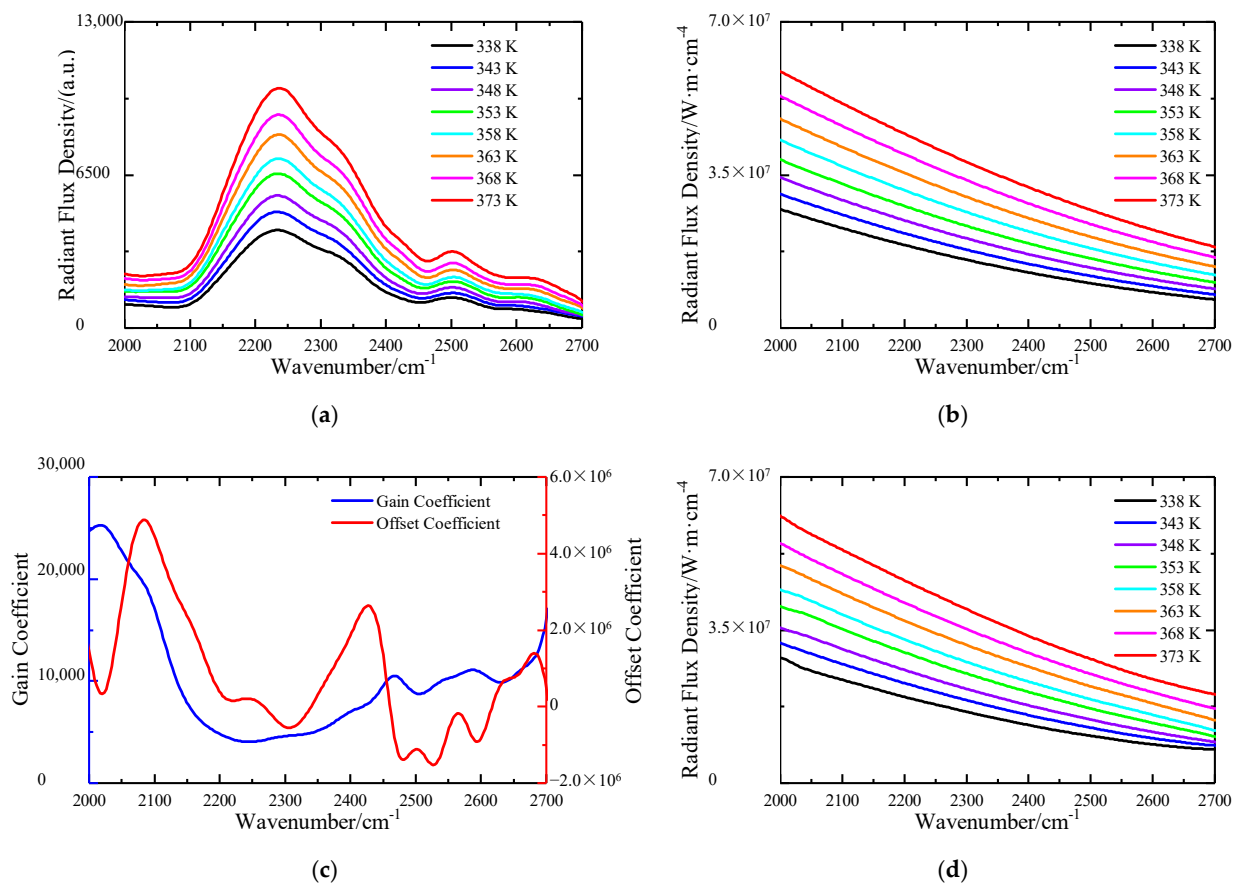


**Figure 16.** (a) Measured spectral response of blackbody at different temperatures. (b) Theoretical blackbody radiation. (c) Spectral response calibration coefficient. (d) Measured spectral response of blackbody after calibration.

Figure 17a shows that the measured central wavenumber of the acetonitrile was  $2273.8\text{ cm}^{-1}$ , and the error from the theoretical value of  $2273\text{ cm}^{-1}$  was only 0.035%. Figure 17b shows that the relative error between the blackbody spectrum after the spectral response calibration and the theoretical value was 4.49%, and the relative error was further reduced to 2.01% after the relative radiation response calibration. It can be seen that the errors of the spectral peak positions and spectral response are higher than the results in Sections 5.2 and 5.3. This is due to the fact that the original data in Sections 5.2 and 5.3 were the actual measured values used to fit the calibration equation, and the errors between their calibration values and the ideal values are mainly fitting error. In contrast, the original data in Section 5.4 were not used to fit the calibration equation, and the error between its calibration value and the ideal value is mainly the prediction error, which is generally higher than the fitting error. Therefore, the spectral wavenumber calibration method, the relative radiation response calibration method, and the spectral response calibration method are effective.

In addition, to explore the effectiveness of the method in practical application, we conducted an outfield experiment at a plant, and the detection area was the emission area of a gas boiler, as shown in Figure 18a. The experimentally acquired original data were processed to obtain the infrared image of the detection region and the transmittance spectrum of the target region as shown in Figure 18b.

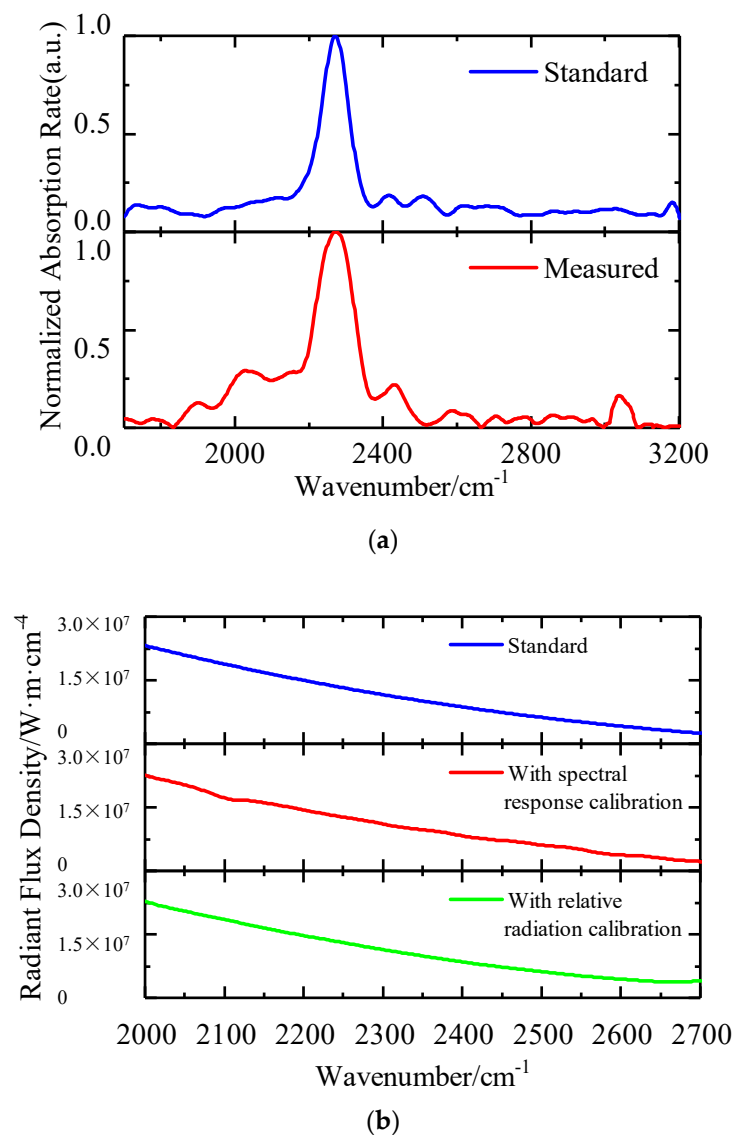
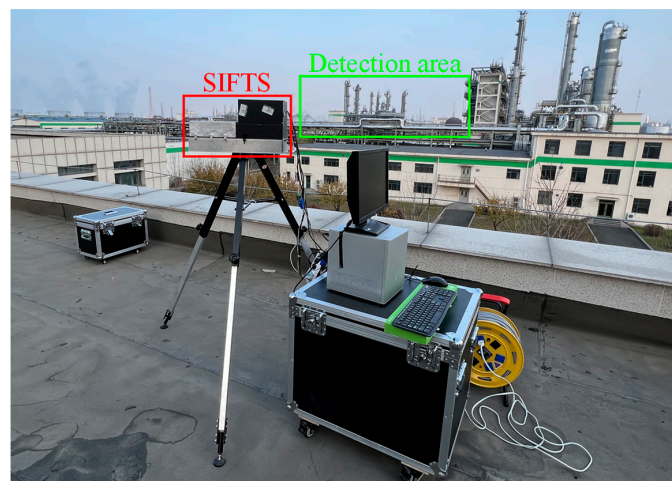
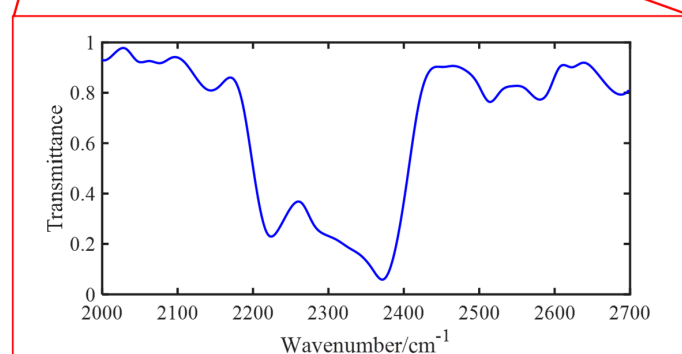
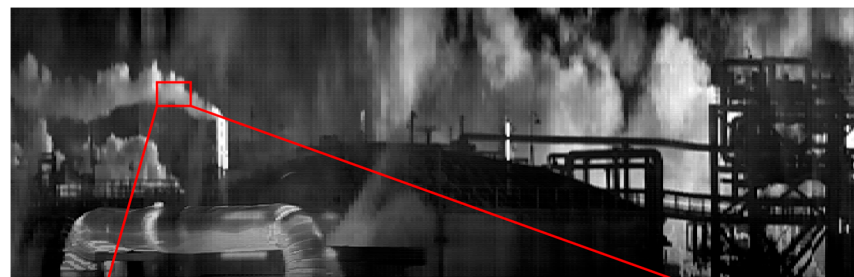


**Figure 17.** (a) Theoretical and measured spectra of acetonitrile. (b) The radiation intensity of blackbody at 333 K.

The target area selected in Figure 18b (in the red box) is the emission from the gas boiler, which typically consists of water vapor, carbon dioxide, oxygen and nitrogen. Among them, only carbon dioxide has a relatively strong absorption peak in the range of 3.7–4.8  $\mu\text{m}$ , specifically in the range of 4.16–4.54  $\mu\text{m}$  (2200–2400  $\text{cm}^{-1}$ ), which is consistent with the results in Figure 18b. Thus, the effectiveness of the method was further validated.



(a)



(b)

**Figure 18.** (a) Field experiment site. (b) The infrared image of the detection region and the transmittance spectrum of the target region.

## 6. Conclusions

For the SIFTS, the systematic error in the interference core has a significant impact on the interferogram and the reconstructed spectrum. In this paper, we divided the systematic error into three types—tilt error, slope error, and rotation error—and established the transfer error model, showing that the systematic error in the interference core will cause a linear shift of the spectral wavenumber, and may also cause an interference fringe rotation of the interferogram. Combined with the transfer error model and instrument principle, we proposed an interferogram and spectrum calibration method combining least square fitting correction and row-by-row FFT-IFFT flat-field correction and built an experimental platform to verify the method.

The experimental results show that the relative radiation response calibration can eliminate the rotation of interference fringes caused by rotation error, and reduce the relative error of the spectral response. Spectral wavenumber calibration can calibrate the wave number linear shift and spectral broadening caused by tilt error and slope error. Spectral

response calibration can calibrate the non-uniform spectral response of the detector in the response band. In general, the method proposed in this paper can improve the detection accuracy of the SIFTS in the data processing stage, and reduce the difficulty of the assembly and adjustment of the interference core to a certain extent. Due to the structural similarity of the interference imaging spectrometer, this method has certain universality.

**Author Contributions:** Conceptualization, B.Z.; methodology, B.Z. and J.L. (Jinguang Lv); software, K.S.; validation, K.Z. and Y.C.; formal analysis, B.Z. and Y.Z.; investigation, K.S.; resources, J.L. (Jingqiu Liang); writing—original draft preparation, B.Z.; writing—review and editing, J.L. (Jinguang Lv) and J.L. (Jingqiu Liang); supervision, W.W.; project administration, Y.Q.; funding acquisition, J.L. (Jinguang Lv) and J.L. (Jingqiu Liang). All authors have read and agreed to the published version of the manuscript.

**Funding:** This research was funded by the National Key R&D Program of China under Grant 2019YFB2006003; funded by the National Natural Science Foundation of China under Grant 61805239, Grant 61627819, Grant 61575193, and Grant 61727818; funded by the Jilin Scientific and Technological Development Program under Grant 20190303063SF, Grant 20180201024GX, and Grant 20150520101JH; funded by the Youth Innovation Promotion Association Foundation of the Chinese Academy of Sciences under Grant 2018254, and 61905240; funded by the National Science and Technology Major Project under Grant 2019QZKK020802.

**Data Availability Statement:** The data presented in this study are available on request from the corresponding author.

**Conflicts of Interest:** The authors declare no conflict of interest. The funders had no role in the design of the study; in the collection, analyses, or interpretation of data; in the writing of the manuscript, or in the decision to publish the results.

## References

1. Griffiths, P.R.; Haseth, J.A. *Fourier Transform Infrared Spectrometry*, 2nd ed.; Wiley: Hoboken, NJ, USA, 1983; pp. 312–314.
2. Yang, C.; Zhou, Z.Y.; Li, Y.; Liu, S.K.; Ge, Z.; Guo, G.C.; Shi, B.S. Angular-spectrum-dependent interference. *Light Sci. Appl.* **2021**, *10*, 217. [[CrossRef](#)]
3. Israelsen, N.M.; Petersen, C.R.; Barh, A.; Jain, D.; Jensen, M.; Hanneschläger, G.; Tidemand-Lichtenberg, P.; Pedersen, C.; Podoleanu, A.; Bang, O. Real-time high-resolution mid-infrared optical coherence tomography. *Light Sci. Appl.* **2019**, *8*, 11. [[CrossRef](#)]
4. Saptari, V. *Fourier Transform Spectroscopy Instrumentation Engineering*, 1st ed.; SPIE Optical Engineering Press: Bellingham, WA, USA, 2003; pp. 4–8.
5. Talghader, J.J.; Gawarikar, A.S.; Shea, R.P. Spectral selectivity in infrared thermal detection. *Light Sci. Appl.* **2012**, *1*, e24. [[CrossRef](#)]
6. Li, A.; Yao, C.; Xia, J.; Wang, H.; Cheng, Q.; Penty, R.; Fainman, Y.; Pan, S. Advances in cost-effective integrated spectrometers. *Light Sci. Appl.* **2022**, *11*, 174. [[CrossRef](#)]
7. Zhang, C.; Zhao, B.; Bin, X.; Li, Y. Interference image spectroscopy for upper atmospheric wind field measurement. *Optik* **2006**, *117*, 265–270. [[CrossRef](#)]
8. Girshovitz, P.; Shaked, N.T. Doubling the field of view in off-axis low-coherence interferometric imaging. *Light Sci. Appl.* **2014**, *3*, e151. [[CrossRef](#)]
9. Pope, A.; Rees, W.G. Impact of spatial, spectral, and radiometric properties of multispectral imagers on glacier surface classification. *Remote Sens. Environ.* **2014**, *141*, 1–13. [[CrossRef](#)]
10. Shang, S.; Lee, Z.; Lin, G.; Hu, C.; Shi, L.; Zhang, Y.; Li, X.; Wu, J.; Yan, J. Sensing an intense phytoplankton bloom in the western Taiwan Strait from radiometric measurements on a UAV. *Remote Sens. Environ.* **2017**, *198*, 85–94. [[CrossRef](#)]
11. Kaiser, F.; Vergyris, P.; Aktas, D.; Babin, C.; Labonté, L.; Tanzilli, S. Quantum enhancement of accuracy and precision in optical interferometry. *Light Sci. Appl.* **2018**, *7*, 17163. [[CrossRef](#)]
12. Zhang, C.; Liu, C.; Chan, K.L.; Hu, Q.; Liu, H.; Li, B.; Xing, C.; Tan, W.; Zhou, H.; Si, F.; et al. First observation of tropospheric nitrogen dioxide from the Environmental Trace Gases Monitoring Instrument onboard the GaoFen-5 satellite. *Light Sci. Appl.* **2020**, *9*, 66. [[CrossRef](#)]
13. Garoi, F.; Garoi, I.; Prepelita, P. Monochromatic light measurement via geometric phase and Fourier-transform spectroscopy method. *Sci. Rep.* **2022**, *12*, 12922. [[CrossRef](#)]
14. Wang, W.; Liang, J.; Liang, Z.; Lü, J.; Qin, Y.; Tian, C.; Wang, W. Design of spatio-temporally modulated static infrared imaging Fourier transform spectrometer. *Opt. Lett.* **2014**, *39*, 4911. [[CrossRef](#)]
15. Zhao, B.; Lv, J.; Ren, J.; Qin, Y.; Tao, J.; Liang, J.; Wang, W. Data processing and performance evaluation of a tempo-spatially mixed modulation imaging Fourier transform spectrometer based on stepped micro-mirror. *Opt. Express* **2020**, *28*, 6320–6335. [[CrossRef](#)]

16. Ren, J.; Lv, J.; Zhao, B.; Wang, Q.; Qin, Y.; Tao, J.; Liang, J.; Wang, W. Optical Design and Investigation of a Dual-Interference Channels and Bispectrum Static Fourier-Transform Imaging Spectrometer Based on Stepped Micro-Mirror. *IEEE Access* **2021**, *9*, 81871–81881. [[CrossRef](#)]
17. Xiang, L.B.; Yang, J.F.; Gao, Z.; Liu, G.X. On the tolerance of the mirror tilting in Fourier transform interferometer. *Acta Photonica Sin.* **1997**, *26*, 132–135.
18. Gao, X.F.; Cui, Y.; Xiang, L.B. The tolerance of the end mirror tilting in high speed rotary spectrometer. *Acta Photonica Sin.* **2006**, *35*, 614–617.
19. Zeng, L.B.; Yin, B.S.; He, B.; Gong, D. Error analysis of moving mirror in Fourier transform interferometer. *Opt. Precis. Eng.* **2006**, *14*, 191–196.
20. Liu, B.; Zhu, Y.; Chen, J.; Wei, W.; Zhang, J.; Wang, N. Analysis of Tolerance of Tilting Mirror and Experiment in Novel Fourier Transform Spectrometer. *Acta Photonica Sin.* **2013**, *42*, 315–319. [[CrossRef](#)]
21. Feng, M.C.; Xu, L.; Jin, L.; Liu, W.Q.; Gao, M.G.; Li, S.; Li, X.X.; Tong, J.J.; Liu, J.G. Tilt and dynamic alignment for the moving mirror in the Fourier transform infrared. *Acta Photonica Sin.* **2016**, *45*, 0412005. [[CrossRef](#)]
22. Barnett, P.D.; Strange, K.A.; Angel, S.M. Improving Spectral Results Using Row-by-Row Fourier Transform of Spatial Heterodyne Raman Spectrometer Interferogram. *Appl. Spectrosc.* **2017**, *71*, 1380–1386. [[CrossRef](#)]
23. Jin, W.; Chen, D.H.; Li, Z.W.; Luo, H.Y.; Hong, J. Alignment error analysis of detector array for spatial heterodyne spectrometer. *Appl. Opt.* **2017**, *56*, 9830–9836. [[CrossRef](#)] [[PubMed](#)]
24. Zou, Y.; Zhang, L.; Han, C.; Li, L. Study of high accuracy spectral calibration of Fourier transform spectrometer. *Spectrosc. Spectr. Anal.* **2018**, *38*, 1268–1275.
25. Feng, X.; Han, C.; Zou, Y.; Chen, B. On-Orbit Spectral Calibration Algorithm of Infrared Fourier Transform Spectrometer. *Acta Opt. Sin.* **2019**, *39*, 0630002. [[CrossRef](#)]
26. Cui, J.; Zhu, J.; Cui, H.; Ma, T. Research on the radiation calibration of micro spectrometer. *Laser Infrared.* **2019**, *49*, 881–885.
27. Lv, Y.; Cong, M.; Tang, Y.; Niu, K.; Zhao, Y. Application of on-orbit radiometric calibration technology for interferometric imaging spectrometer. *J. Harbin Inst. Technol.* **2022**, *54*, 17.
28. Smith, B.W.; Harlander, J.M. Imaging spatial heterodyne spectroscopy: Theory and practice. *Infrared Technol. Appl.* **XXV SPIE** **1999**, 3698, 925–931.
29. Harlander, J.M.; Roesler, F.L.; Englert, C.R.; Cardon, J.G.; Wimperis, J. Spatial heterodyne spectroscopy for high spectral resolution space-based remote sensing. *Opt. Photonics News* **2004**, *15*, 46–51. [[CrossRef](#)]
30. McCormack, E.A.; Mortimer, A.H.; Ciaffoni, L. Compact spatially heterodyned static interferometer. *Appl. Opt.* **2020**, *59*, 4271–4278. [[CrossRef](#)]
31. Ersoy, O.K.; Haseth, J.A. *Diffraction, Fourier Optics and Imaging*, 1st ed.; Wiley: Hoboken, NJ, USA, 2006; pp. 12–14.
32. Li, Z.; Xiong, W.; Shi, H.; Wang, X.; Ye, H.; Wei, Q.; Qiao, Y. Study on laboratory calibration of spatial heterodyne spectrometer. *Acta Opt. Sin.* **2014**, *34*, 0430002.
33. Guo, Q.; Chen, F.; Li, X.; Chen, B.; Wang, X.; Chen, G.; Wei, C. High-accuracy source-independent radiometric calibration with low complexity for infrared photonic sensors. *Light Sci. Appl.* **2021**, *10*, 163. [[CrossRef](#)]

**Disclaimer/Publisher’s Note:** The statements, opinions and data contained in all publications are solely those of the individual author(s) and contributor(s) and not of MDPI and/or the editor(s). MDPI and/or the editor(s) disclaim responsibility for any injury to people or property resulting from any ideas, methods, instructions or products referred to in the content.